

Corrosion Study of Picosecond-Laser Structured and Anodized Ti6Al4V for Bone Screws

Dominik Knapic, Andrei Ionut Mardare, Heike Voss, Jörn Bonse, and Achim Walter Hassel*

A corrosion study is performed on six variations of titanium grade 5 (Ti6Al4V) samples. Samples are prepared in different conditions by variation of pre-anodization, postanodization, and picosecond-laser (ps-laser) surface treatment, while polished and anodized samples serve as reference. Microcones and nanosized periodic surface features are successfully produced on Ti6Al4V samples. The morphology and topography of the structures are visualized by scanning electron microscopy and white light interference microscopy. Furthermore, the relative electrochemically active surface area (ECSA) is determined for the ps-laser-treated samples. It is determined that the preanodized and laser-treated sample has 3.5 times larger ECSA than a polished sample, and that the laser-treated sample has 4.1 times larger area. Moreover, Tafel analysis is performed to determine the corrosion properties of the samples. It is shown that the corrosion resistance improves for both laser-structured samples after the anodization. To further study the surface of the samples, electrochemical impedance spectroscopy measurements are conducted. The study indicates that the ps-laser-treated and anodized Ti6Al4V is suitable to be used for the fabrication of bone screws and plates due to its improved corrosion resistance as compared to nonanodized samples.

1. Introduction

In recent times, an increased interest in bone implant research has been seen in the scientific community. A demand for research in this field has been fueled by an industry which already reached a global market value for bone implants of 105 billion US \$.^[1] Materials used for bone implant manufacturing have to be biocompatible and have to comply with very strict requirements to be approved for use in the human body.^[2] Besides biocompatibility and mechanical properties, one of the most important properties of the bone implant is its corrosion resistance to prevent inflammations, and poisoning, and to assure the overall functionality of the implant.^[3,4] Titanium grade 5 alloy (Ti6Al4V) is a biocompatible material commonly used for bone implants such as bone screws and plates. It has become an industry standard in recent years. Unlike dental implants that require improved osseointegration and permanent contact with the bone, bone


screws, and plates normally have to be explanted soon after the surgery to allow full bone healing. This requires the surface of the plate or screw to be osseorepellent for easier and less traumatic removal. Osseorepellent surfaces can be produced by altering the surface of an implant at macro- and nanoscale, changing its roughness, chemistry, and morphology. There are various techniques that can be used for this purpose, such as glancing angle deposition,^[5–7] anodization,^[8–14] sand-blasting,^[15] etching,^[16,17] and ultrashort laser processing.^[12,13,18–20]

Ultrashort pulsed laser treatment can produce specific surface structures, their scale, and their morphology depending on the processing parameters. Some of these structures are called laser-induced periodic surface structures (LIPSS). They form in a self-ordered way and manifest as grating-like periodic line structures with periods far smaller than the irradiated laser spot diameters. LIPSS are distinguished by the ratio of their spatial period and the laser irradiation wavelength. They are classified as high spatial frequency LIPSS (HSFL), which have periods significantly smaller than the irradiation wavelength, and low spatial frequency LIPSS (LSFL), which have near-wavelength periods.^[21,22] For most metals (and also for titanium alloys), the LSFL are dominant and oriented perpendicular to the linear polarization of the laser beam, caused by electromagnetic scattering and

D. Knapic, A. I. Mardare, A. W. Hassel
Institute of Chemical Technology of Inorganic Materials
Johannes Kepler University Linz
Altenberger Str. 69, 4040 Linz, Austria
E-mail: achimwalter.hassel@jku.at

H. Voss, J. Bonse
Bundesanstalt für Materialforschung und –prüfung (BAM)
Unter den Eichen 87, 12205 Berlin, Germany

A. W. Hassel
Department of Physics and Chemistry of Materials, Faculty of Medicine
and Dentistry
Danube Private University
Steiner Landstraße 124, Krems an der Donau 3500, Austria

 The ORCID identification number(s) for the author(s) of this article can be found under <https://doi.org/10.1002/pssa.202300609>.

© 2024 The Authors. physica status solidi (a) applications and materials science published by Wiley-VCH GmbH. This is an open access article under the terms of the Creative Commons Attribution-NonCommercial-NoDerivs License, which permits use and distribution in any medium, provided the original work is properly cited, the use is non-commercial and no modifications or adaptations are made.

DOI: 10.1002/pssa.202300609

interference effects at the microscopically rough sample surface.^[23] When using a spatially Gaussian intensity distribution in a laser beam scanning approach for the laser treatment, hierarchical micro-nanostructures can be straightforwardly processed at the sample surface. Furthermore, the high-intensity part of the laser beam generates micrometric cones (so-called spikes), which are subsequently “overwritten” by LSFL through the following low-intensity wing of the Gaussian intensity distribution.^[24]

During the picosecond-laser (ps-laser) treatment, the surface melts locally and is immediately oxidized if exposed to an oxygen-rich atmosphere. In such environment, an imperfect oxide layer with a high number of defects is grown, therefore enabling an additionally anodic oxidation which further alters the surface.^[12] The surface structure manipulation also has an influence on the corrosion resistance, which is crucial for medical implants, as the conditions in a human body could facilitate increased corrosion probability due to increased temperature, non-neutral pH, exposure to corrosive ions, and the possibility of organic matter adsorption.^[3,4,25]

The aim of this work was to determine the corrosion properties of ps-laser-treated and anodized (preanodized and postanodized) Ti grade 5 (Ti6Al4V) and to compare them to only polished and anodized Ti6Al4V samples, which are currently used as an industry standard. The samples were first analyzed by scanning electron microscopy (SEM) and white light interference microscopy (WLIM) to determine their superficial morphology and surface roughness. Next, the relative electrochemically active surface area (ECSA) was coulometrically determined for the ps-laser-treated samples by comparing the total exchanged charge used in a series of voltammetry cycles with a polished Ti6Al4V sample as a reference. Moreover, to determine the corrosion resistance, potentiodynamic polarization curves were studied, and Tafel analysis was performed. To further study the oxide properties, electrochemical impedance spectroscopy (EIS) measurements were done and the experimental data were fitted to proposed electrical circuit models.

2. Experimental Section

2.1. Sample Preparation

Titanium grade 5 (Ti6Al4V) (Hempel metals, Dübendorf, Switzerland) round plates (diameter $d = 22$ mm) were first ground with 220, 400, 600, 1000, 2500, and 4000 grit number sandpapers. After the grinding, the samples were polished with silica solution (50 nm) producing a mirror-like surface. Before further processing, the samples were cleaned in an ultrasonic bath with isopropanol and distilled water, consequently. Afterward, 3 variants of samples were prepared, and one set was additionally anodized, thus obtaining 6 different samples, as presented in **Table 1**. The preanodization was done potentiostatically. A two-electrode setup was used for the potentiostatic anodization. The setup consisted of a TDK lambda Z+ power supply connected in series with a Keysight 34460A digital multimeter. The system was controlled via custom-made software which was developed in LabVIEW. Titanium grade 5 samples were preanodized in 3 M H₃PO₄, at 95 V for 100 s. A preanodization potential of 95 V which produces the oxide layer of approximately 162 nm

Table 1. Variations of the produced samples. The polished 0V sample is only polished metal without any additional treatment, while polished 95 V was also preanodized. Sample 0V0V is only ps-laser-treated, while 0V10V was additionally postanodized. Sample 95V0V was preanodized and ps-laser-treated, while the sample 95V10V was preanodized, ps-laser-treated, and postanodized.

Sample	Potentiostatic/ preanodization	ps-laser treatment	Potentiodynamic/ postanodization
Polished 0V	–	–	–
Polished 95 V	+	–	–
0V0V	–	+	–
0V10V	–	+	+
95V0V	+	+	–
95V10V	+	+	+

($k = 1.7 \text{ nm V}^{-1}$) was chosen according to the commercial bone plates which have similar thicknesses. Moreover, the postanodization was done potentiodynamically. The samples were anodized in 0.1 M H₂SO₄, up to 10 V with a rate of potential increase of 100 mV s⁻¹ in a classical 3 electrode setup. Here, the thickness of the produced oxide according to the $k = 1.7 \text{ nm V}^{-1}$ is approximately 17 nm. This potential and its corresponding thickness were chosen not to reduce the impact on the nanostructure morphology produced by the laser treatment whose dimensions are approximately 500 nm in period. The ps-laser treatment was performed with a TRUMPF Trumicro 5050 femtoedition laser system with a pulse duration of 925 fs at 1030 nm wavelength. The laser was focused to a 114 μm spot diameter and deflected with an X–Y Galvo-scanner system equipped with an F-Theta-lens. Four areas of 3 \times 3 mm² per sample plate were treated in a meandering way with 73.2 μJ pulse energy, a scanning speed of 49.5 mm s⁻¹, and a line offset of 40 μm at 80 kHz pulse repetition rate. All further measurements done on the laser-processed samples were performed after 1 month of the treatment.

2.2. Surface Characterization

The surface morphology of the structures obtained by the ps-laser treatment was characterized with a ZEISS Supra 40 SEM, operated at 10 kV electron acceleration voltage in In-Lens mode.

The surface topography was analyzed by white light interference microscopy (WLIM) using a NexView from Zygo (Middlefield, USA) with a 20 \times Mirau interferometer objective with a lateral optical resolution of 0.7 μm . For a statistical assessment of the surface roughness, areas of 420 \times 420 μm^2 were characterized and 14 cross-sections were acquired in the direction perpendicular to the laser scanning lines. The cross-sections were used to calculate values of the average surface roughness R_a and the maximum height (R_z) of the laser-processed spikes along with the corresponding mean values.

2.3. Electrochemical Measurements

All electrochemical measurements including the potentiodynamic anodization were performed in a classical 3 electrode

setup consisting of a CompactStat potentiostat (Ivium Technologies, Eindhoven, The Netherlands), a platinum mesh served as a counter electrode, an Ag |AgCl| 3 M KCl as reference electrode, and the titanium grade 5 sample as working electrode. To determine the ECSA of the laser-structured samples, a series of cyclic voltammograms (CV) from $E_{vs\ SHE} = 1.00\text{ V}$ to $E_{vs\ SHE} = 5.00\text{ V}$ in steps of 0.25 V was performed in a $0.1\text{ M H}_2\text{SO}_4$ solution. Next, the total exchanged charge during the CVs was compared with the one obtained from a polished sample which was used as a reference. Furthermore, the EIS was performed in Ringer's solution after 1 h immersion to enable good contact with the electrolyte and to achieve a stable measurement system. The Ringer's solution^[26] consisted of 8.6 g dm^{-3} NaCl, 0.3 g dm^{-3} KCl, and 0.25 g dm^{-3} CaCl₂ in ultra-pure distilled water and was chosen because it is one of the standard human body liquid simulations. The frequency range was defined from 10^5 to 10^{-2} Hz. The acquired data were analyzed and modeled in ZView. Finally, the Tafel plots were measured in Ringer's solution after 1 h immersion. First, the corrosion potential (E_{corr}) was determined. Second, the potentiodynamic polarization curves were swept between $\pm 10\text{ mV}$ from the obtained E_{corr} . The Tafel plots were further analyzed using the Ivium Software.

3. Results and Discussion

3.1. Surface Characterization

The SEM micrographs of the ps-laser-treated areas depicted in **Figure 1** show well-separated hierarchical micrometric spikes, covered with pronounced nanometric LSFL on top of the spikes along with a uniform height distribution, visualized for all six different samples listed in Table 1 (arranged in columns) and

at four different magnifications (corresponding to the individual rows). The laser-induced spikes generated on the polished surface (polished and laser, 0V0V) have an average height of $\approx 19\ \mu\text{m}$ as measured by WLM (see **Figure 2**). Importantly, the anodization state of the sample surface (0V0V, 95V0V, 0V10V, or 95V10V) does not significantly influence the surface morphology that is ruled here by the laser processing conditions. The same applies to the polished reference surfaces. In other words, the presence of pre- or postanodized oxide layers on the Ti6Al4V does not significantly affect the final (laser-processed) surface morphologies here.

3.2. ECSA

Figure 3a,b shows CV series which were used to determine the relative ECSA. In **Figure 3a**, the shift of the anodic onset can be seen after each cycle. According to the high field model,^[27] this happens because after each cycle an additional anodic oxide is grown, making it thicker and thus requiring higher potential to onset the anodic growth. This is seen by the current increases exactly at the potential peak of the previous cycle. The ECSA ratios of the preanodized (95V0V) and laser-treated sample (0V0V) were determined coulometrically by comparing the exchanged charge in each cycle with the one obtained from the polished sample (polished 0 V) taken as reference. This is possible because the exchanged charge used for the anodic growth is directly proportional to the surface of the samples, similar approach was already reported in ref. [13]. The exchanged charge Q is calculated by integrating the time dependence of the current evolution measured in the CV curve. **Figure 3b** shows the CV cycles that were used to determine the relative ECSA, taking into account only the anodic oxide growth reaction. An average of the

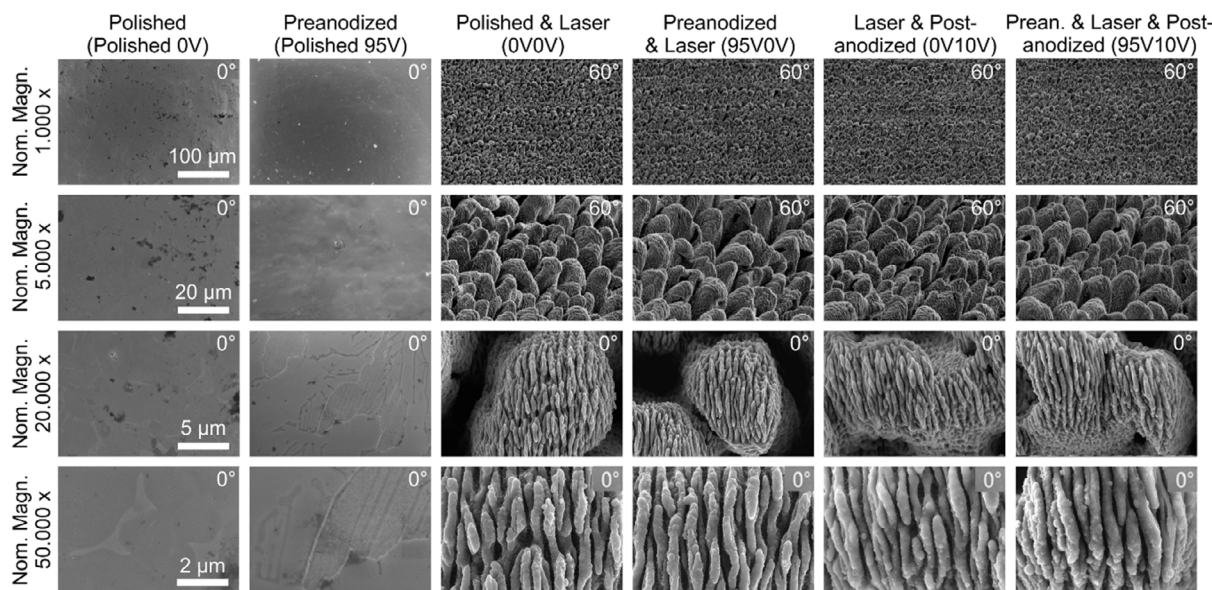


Figure 1. Collage of SEM micrographs of ps-laser processed areas on all six samples (columns) at four different rising magnifications (rows). The first two columns depict the polished surfaces as a reference. The third column shows hierarchical spikes processed on the 0V0V sample, followed by the 95V0V, 0V10V, and 95V10V samples, respectively. Some micrographs were imaged by tilting the sample 60° relative to the surface normal, the other micrographs were taken under normal incidence (as indicated in the upper right corners). For each nominal magnification (row), a joint white scale bar is included in the left micrograph.

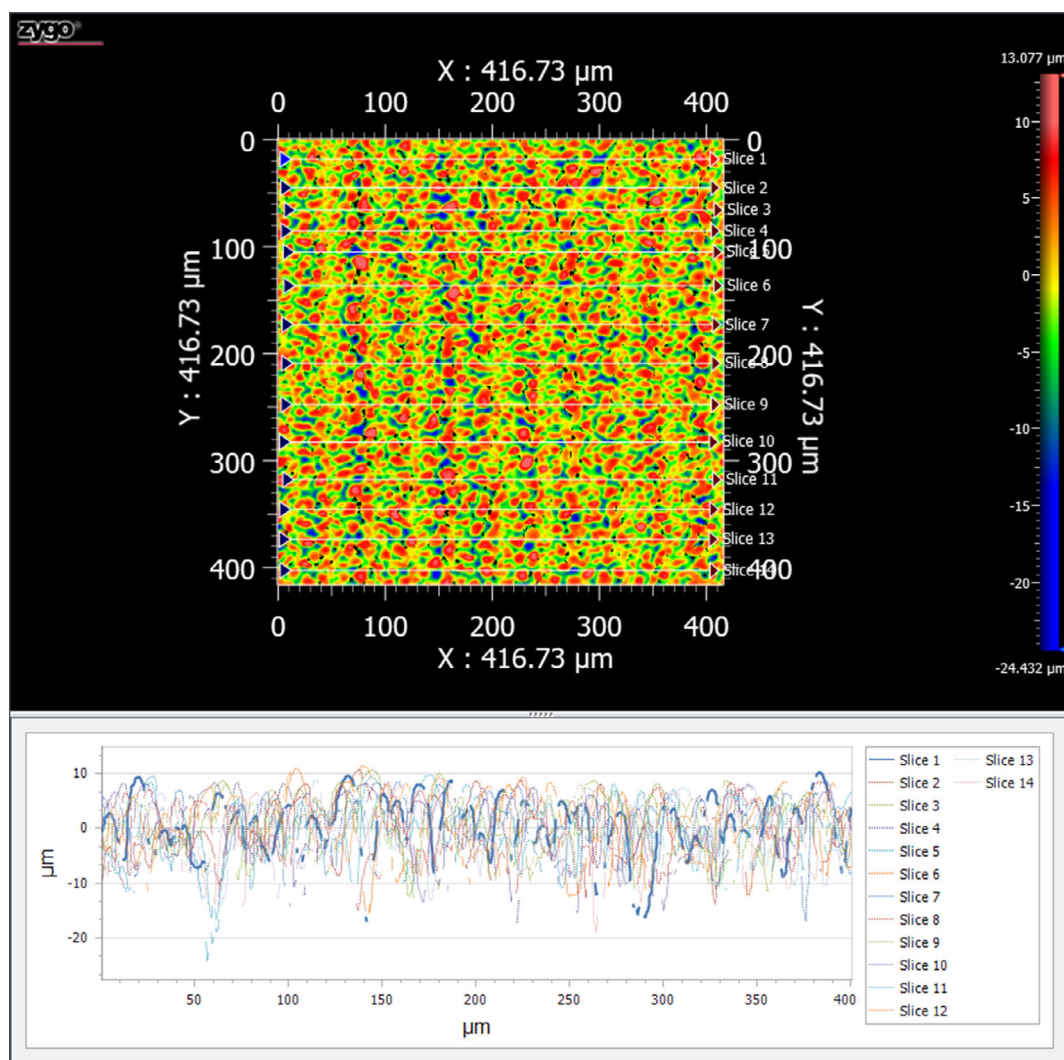


Figure 2. Surface topography of the spikes processed by ps-laser irradiation on the polished sample surface (0V0V) as measured by WLIM (top). The 14 different vertical white lines mark the positions, where cross-sections (slices) were acquired (bottom). The slices' individual roughness parameter values range between $R_a = 3.88$ and $4.52 \mu\text{m}$ (R_z between 17.84 and $20.40 \mu\text{m}$), resulting in corresponding mean value of $R_{a,\text{mean}} = 4.22 \pm 0.19$ and $R_{z,\text{mean}} = 19.32 \pm 0.70 \mu\text{m}$.

exchanged charge used in each cycle in a potential range between 1.75 and 2.75 V versus standard hydrogen electrode (SHE) was taken into account because in this range almost 100% of the exchanged charge is used for the anodic oxide growth. It was found that the laser-treated sample (0V0V) has an ECSA 4.1 times larger than the polished sample (polished 0 V). However, the ECSA of the preanodized sample is only 3.5 times larger, as presented in Figure 3d. This 17% difference between the ECSA values indicates that the oxide produced by the ps-laser on the preanodized sample (95V0V) has less defects than the laser-treated one (0V0V), which could be “healed” by additional anodization. In this context, the oxide “healing” refers to the reduction of the defects from the laser-induced thermal oxidation by the subsequent anodization. In contrast to the laser-treated sample (0V0V), the ps-laser treatment on the preanodized sample (95V0V) was done on an already anodized surface. Taking into account an oxide forming factor k of 1.7 nm V^{-1} ,^[27–30] and the

potential of 95 V the thickness of the oxide is calculated as 162 nm by their multiplication. This explains the different amounts of the exchanged charge used for “healing” of the laser-formed oxide. Furthermore, the oxygen evolution potential for ps-laser-treated and polished samples was determined by analyzing the CVs. As observable in Figure 3a,c, the increase in the current and exchanged charge Q starts in the range of 2.75 – 3.00 V, which indicates the start of the oxygen evolution reaction, as already reported in ref. [31]. The current below the threshold of 2.75 – 3.00 V is predominantly ionic as a result of anodic oxide growth, whereas after the threshold value, additional electronic current is introduced due to oxygen evolution. As it can be seen in Figure 3c, there is a significant difference in exchanged charge ratio between ps-laser-treated and polished sample after the identified potential range for oxygen evolution. The ratio of the exchanged charge reaches the maximum value of 20 at a potential of $E_{\text{vs SHE}} = 3.75$ V. This increased oxygen evolution for the

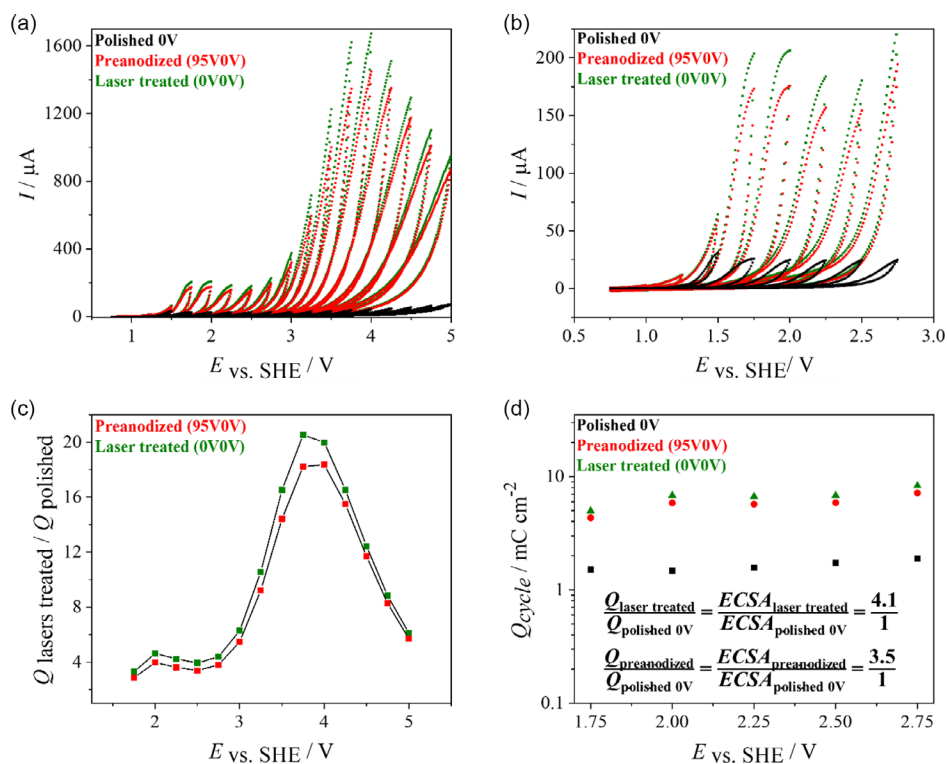


Figure 3. a) Series of CV for polished 0V, preanodized (95V0V), and ps-laser-treated sample (0V0V). b) Series of CV in the potential range from $E_{vs\ SHE} = 1.25\text{--}2.75\text{ V}$. c) $Q_{\text{laser treated}}/Q_{\text{polished}}$ ratio for the preanodized (95V0V) and ps-laser-treated sample (0V0V). d) Total exchanged charge Q for the CV cycles in the potential range of $E_{vs\ SHE} = 1.25\text{--}2.75\text{ V}$. The CV cycles were performed at a scan rate of 100 mV s^{-1} in $0.1\text{ M H}_2\text{SO}_4$.

ps-laser-treated samples is associated with a catalytic effect related to the nano- and microsurface structure and the specific surface morphology. The increased ECSA due to the nano- and microsurface structuring provides more catalytic sites, while specific surface morphology provides better access to them.^[32]

3.3. Tafel Analysis

Figure 4 shows the Tafel plots for all of the studied variations of the Ti6Al4V measured in Ringer's solution and $E_{\text{corrosion}}$, $I_{\text{corrosion}}$, and corrosion rate values for the analyzed samples. Tafel analysis is a standard procedure for corrosion resistance studies, it provides the $E_{\text{corrosion}}$ value which shows at which potential the corrosion occurs, and the $I_{\text{corrosion}}$ value which shows the rate of the corrosion. In general, for implants, a high value is desired for the $E_{\text{corrosion}}$ and for $I_{\text{corrosion}}$ a lower value. It can be seen that $E_{\text{corrosion}}$ is increased for each sample after the anodization and it is in the range of $E_{\text{corrosion vs SHE}} = 0.52\text{--}0.53\text{ V}$. Additionally, comparing the 0V0V and 95V0V, a higher value of $E_{\text{corrosion vs SHE}}$ was found for the preanodized sample which can be explained by lower number of defects in the oxide layer of the preanodized sample. This also correlates to the results in the ECSA section. The lowest value of $E_{\text{corrosion vs SHE}} = -0.43\text{ V}$ was measured for the polished 0V sample. Moreover, $I_{\text{corrosion}}$ values were also improved with additional anodization for each sample. The highest value was measured for polished 0V and the lowest for polished 95V sample. The corrosion rate is directly

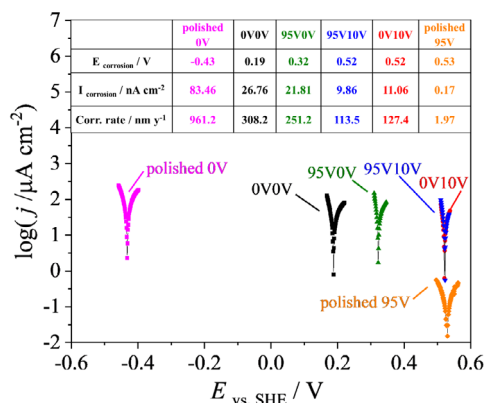


Figure 4. Tafel plots of polished and ps-laser-treated Ti6Al4V samples measured in Ringer's solution and the corrosion parameters of the samples obtained from the Tafel analysis in Ivium software.

correlated to the $I_{\text{corrosion}}$. The values of both the corrosion rate and the $I_{\text{corrosion}}$ for the ps-laser-treated samples are 2 orders of magnitude larger than for the polished 95V, and the polished 0V sample is 3 orders of magnitude larger. Due to the relatively short time of maximum of several months that a bone screw or a bone plate is inside of the human body this is an acceptable corrosion rate. To conclude, the anodization of the ps-laser-structured samples increases their corrosion resistance and the bone screws and plates made using this procedure are suitable

for a short-term implantation in the range of up to several months.

3.4. EIS

Figure 5 shows experimental and fitted EIS data for all sample variations and the models that were used for data fitting. The classical Randles circuit was used for fitting of the results obtained from the polished 0 V sample, as presented in Figure 5a. The Randles circuit with the additional Warburg element was used for fitting the data obtained from all laser-structured samples and the polished 95 V, as shown in Figure 5b. Generally, the Warburg element describes systems that are diffusion-controlled due to their high porosity and roughness.^[33] In the present study, the Randles circuit with a Warburg element describes these systems very well due to the high roughness and porosity of the laser-treated samples, as observable in the impedance (Z) and phase shift (ϕ) vs frequency plots displayed in Figure 5c,d. High surface roughness and porosity for the laser-treated samples are shown in Figure 1, and were reported in other studies.^[12–14,18] Moreover, the reasoning behind the use of a model with the diffusion dominated conduction (Warburg element) for the polished 95 V sample is supported by the assumption of the inner nanoporosity which is likely formed by potentiostatic anodization. Due to the very short time of the anodic oxide growth for the potentiostatic anodization, inner porosity can form because of initial surface roughness.^[30,34] Models using the Warburg element were already reported for anodized Ti6Al4V.^[35]

In Table 2, the model parameters are presented for all of the laser-treated and polished samples. Comparing the electrolyte resistance R_s values for laser-structured and the polished samples, a significant difference is spotted. This difference in measured electrolyte resistance could be due to the diminished contact between the electrolyte and the surface of the samples. Because of their hydrophobicity which was observed during experiments, air pockets are developed at the electrolyte/sample interface increasing the measured resistance. The hydrophobicity of the fs-laser-treated samples was also reported in other studies.^[18] Moreover, it was reported that the laser-treated samples changed from hydrophilic to hydrophobic with time after exposure to air.^[36] The total resistance R_{total} of the samples shows the highest value for the polished 95 V sample and the lowest value for the 0V0V sample. The lowest resistance measured for 0V0V sample indicates an oxide layer with a higher number of defects which is in agreement with the highest value of constant phase element (CPE). A higher CPE value correlates to higher capacitance. This indicates defects and heterogeneity in the oxide where the charge can be stored, thus increasing the capacitance and consequently the CPE value. The highest resistance value for a polished 95 V sample indicates a thick compact oxide layer with low number of defects which is supported by the lowest CPE value of 0.17. For the ps-laser-structured samples, in each case after the anodization the total resistance increased which indicates less defects in the oxide layer due to the anodic oxide “healing.” While comparing these results to the corrosion resistance, the same behavior can be spotted in increased corrosion resistance after the anodization. This shows the correlation between the “healed” oxide with less defects and its improved corrosion

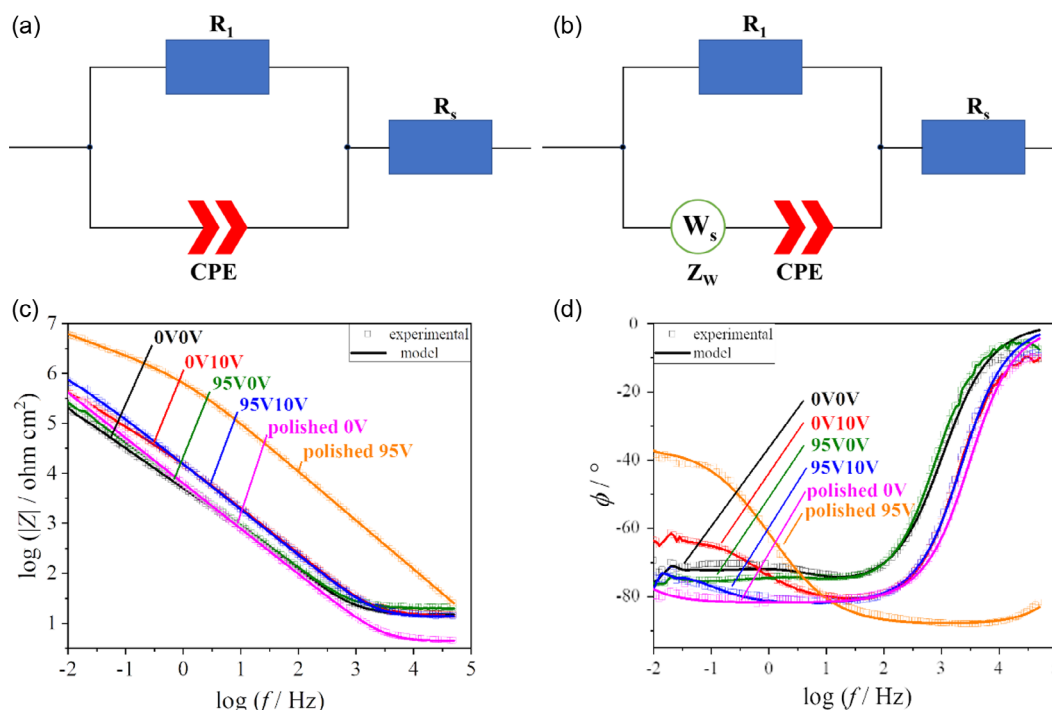


Figure 5. Equivalent circuits used for experimental data fitting. a) Classical Randles circuit used for fitting of polished 0 V sample. b) Modified Randles circuit with additional Warburg element used for fitting of all ps-laser-treated samples and a polished 95 V sample. EIS spectra of the polished and ps-laser-treated Ti6Al4V samples. c) $\log(|Z|)$ versus $\log(f)$. d) Phase shift ϕ versus $\log(f)$.

Table 2. The values of the circuit elements obtained from the models in ZView software.

	$R_s / \Omega \text{ cm}^2$	Error / %	$\text{CPE} / \mu\Omega^{-1} \text{ s}^n \text{ cm}^2$	Error / %	$n / 1$	Error / %	$R_1 / \text{M}\Omega \text{ cm}^2$	Error / %	$W_s - R / \text{M}\Omega \text{ cm}^2$	Error %	$R_{\text{total}} / \text{M}\Omega \text{ cm}^2$
0V0V	14.78	0.6	34.28	2.3	0.86	0.4	0.01	22.1	1.27	8.6	1.28
0V10V	14.21	0.5	11.27	0.9	0.91	0.2	0.06	8.5	1.93	9.0	1.99
95V0V	19.88	0.4	26.68	1.9	0.88	0.3	0.01	16.4	2.32	6.6	2.33
95V10V	13.5	0.5	12.06	0.5	0.91	0.1	0.90	9.5	6.53	8.5	7.42
Polished 0 V	4.37	0.6	29.66	0.4	0.91	0.1	5.94	18.8			5.94
Polished 95 V	2.17	8.2	0.17	0.7	0.98	0.1	0.35	6.7	16.03	8.1	16.38

resistance. When the total resistance values of the ps-laser-treated samples are compared with each other it is seen that the pre-anodized samples have higher values due to less defects, as previously discussed for the total exchanged charge. This is also supported by the lower CPE value of the preanodized sample, indicating less defects in the oxide. The polished 0 V sample showed a higher CPE value than all of the laser-structured samples except the 0V0V. This is explained by the fact that a polished 0 V sample has a compact native oxide layer. The CPE value of the polished 0 V sample is comparable with the not postanodized ps-laser-treated samples (0V0V, 95V0V). In this case, the relatively high CPE value does not indicate defects in the oxide. The relatively high value is present here due to the low thickness of the native oxide layer, which is typically between 4 nm and 10 nm.^[27,37]

4. Conclusion

Hierarchical surface structures of desired morphology, i.e., microcones covered with nanosized LIPSS features were produced on polished Ti6Al4V samples. The morphology of the structures was studied by SEM, while its topography and roughness was characterized by WLIM. Furthermore, the relative ECSA was determined for the ps-laser-treated samples. It was found that the laser-treated sample (0V0V) has the ECSA 4.1 times larger than the polished reference sample (polished 0 V), while a preanodized sample has only 3.5 times larger area. It was concluded that the difference in the area is due to the lower number of defects in the oxide produced by the laser for the preanodized sample (95V0V). Moreover, the Tafel analysis was done to determine the corrosion properties of the samples. It was shown that the corrosion resistance improved for both laser-structured samples after the anodization. Comparing the 0V0V and 95V0V samples, a higher value of $E_{\text{corrosion vs SHE}}$ was measured for the preanodized sample, which can be explained by the lower number of defects in the oxide layer of the preanodized sample. To further study the surface of the samples, EIS measurements were conducted. The data were fitted to the proposed equivalent circuits. The classical Randles circuit was used for the polished 0 V sample, whereas for all other samples, the modified Randles circuit with the additional Warburg element was used. The highest total resistance R_{total} was measured for the polished 95 V sample. For both of the ps-laser-treated samples, the total resistance increased after the anodization. Additionally, the CPE values were in both cases lower for the anodized laser samples (0V10V, 95V10V) which is explained by the “healing” of the laser-induced

oxide, thus reducing the number of defects in it. Moreover, this is also supported by the lower CPE value of the preanodized sample, indicating less defects in the oxide. Finally, it is concluded that the ps-laser-treated and additionally anodized Ti6Al4V showed improved corrosion resistance, thus making them suitable for use as bone screws and plates.

Acknowledgements

The authors acknowledge the LaserImplant project funded by the European Union Horizon 2020 research and innovation program under grant agreement number 951730. The authors are indebted to Johannes Heitz (JKU) who served as coordinator of this project. The authors would like to thank S. Benemann (BAM 6.1) for the SEM characterization and M. Weise (BAM 6.1) for the WLIM measurements.

Conflict of Interest

The authors declare no conflict of interest.

Data Availability Statement

Research data are not shared.

Keywords

anodization, bone screws, implant material, laser-induced periodic surface structures, titanium alloys

Received: August 11, 2023

Revised: January 22, 2024

Published online:

- [1] N. Sirdeshmukh, G. Dongre, *Mater. Today: Proc.* **2021**, *44*, 2348.
- [2] *Mechanical Testing of Orthopaedic Implants* (Ed: E. A. Friis), Elsevier Science, Kent, MI **2017**.
- [3] S. Zhou, J. Wang, P. Cai, *Int. J. Electrochem. Sci.* **2017**, *12*, 7174.
- [4] L. Zhu, X. Tong, Z. Ye, Z. Lin, T. Zhou, S. Huang, Y. Li, J. Lin, C. Wen, J. Ma, *Chem. Eng. J.* **2022**, *450*, 137946.
- [5] A. I. Mardare, S. Huber, C. C. Mardare, E. Bradt, S. Hild, A. W. Hassel, *Appl. Surf. Sci.* **2020**, *499*, 143943.
- [6] Y. Motemani, C. Greulich, C. Khare, M. Lopian, P. J. S. Buenconsejo, T. A. Schildhauer, A. Ludwig, M. Köller, *Appl. Surf. Sci.* **2014**, *292*, 626.
- [7] N. Ziegler, C. Sengstock, V. Mai, T. A. Schildhauer, M. Köller, A. Ludwig, *Nanomaterials* **2019**, *9*, 60.

- [8] H. A. Acciari, D. P. Palma, E. N. Codaro, Q. Zhou, J. Wang, Y. Ling, J. Zhang, Z. Zhang, *Appl. Surf. Sci.* **2019**, *487*, 1111.
- [9] J. Alipal, T. C. Lee, P. Koshy, H. Z. Abdullah, M. I. Idris, *Heliyon* **2021**, *7*, e07408.
- [10] S. E. Kim, J. H. Lim, S. C. Lee, S.-C. Nam, H.-G. Kang, J. Choi, *Electrochim. Acta* **2008**, *53*, 4846.
- [11] D. Krupa, J. Baszkiewicz, J. W. Sobczak, A. Biliński, A. Barcz, B. Rajchel, *Vacuum* **2003**, *70*, 109.
- [12] M. Muck, B. Wolfsjäger, K. Seibert, C. Maier, S. A. Lone, A. W. Hassel, W. Baumgartner, J. Heitz, *Nanomaterials* **2021**, *11*, 1342.
- [13] S. A. Lone, M. Muck, P. Fosodeder, C. C. Mardare, C. Florian, A. Weth, J. Krüger, C. Steinwender, W. Baumgartner, J. Bonse, J. Heitz, A. W. Hassel, *Phys. Status Solidi A* **2020**, *217*, 1900838.
- [14] D. Knapic, M. Muck, J. Heitz, W. Baumgartner, A. I. Mardare, C. Kleber, A. W. Hassel, *Electrochim. Acta* **2023**, *466*, 142965.
- [15] R. Melentiev, C. Kang, G. Shen, F. Fang, *Wear* **2019**, *428–429*, 111.
- [16] A. E. Medvedev, H. P. Ng, R. Lapovok, Y. Estrin, T. C. Lowe, V. N. Anumalasetty, *J. Mech. Behav. Biomed. Mater.* **2016**, *57*, 55.
- [17] M. Zboun, V. Ansan, N. Topcuoglu, F. Kuruoglu, L. T. Sener, F. Sarcan, *Surf. Interfaces* **2020**, *21*, 100703.
- [18] J. Heitz, C. Plamadeala, M. Muck, O. Armbruster, W. Baumgartner, A. Weth, C. Steinwender, H. Blessberger, J. Kellermaier, S. V. Kirner, J. Krüger, J. Bonse, A. S. Guntner, A. W. Hassel, *Appl. Phys. A* **2017**, *123*, 734.
- [19] A.-C. Joel, M. Meyer, J. Heitz, A. Heiss, D. Park, H. Adamova, W. Baumgartner, *ACS Appl. Nano Mater.* **2020**, *3*, 3395.
- [20] P. Fosodeder, W. Baumgartner, C. Steinwender, A. W. Hassel, C. Florian, J. Bonse, J. Heitz, *Adv. Opt. Technol.* **2020**, *9*, 113.
- [21] J. Bonse, S. Höhm, S. V. Kirner, A. Rosenfeld, J. Krüger, *IEEE J. Sel. Top. Quantum Electron.* **2017**, *23*, 9000615.
- [22] J. Bonse, S. Gräf, *Nanomaterials* **2021**, *11*, 3326.
- [23] J. Bonse, S. Gräf, *Laser Photonics Rev.* **2020**, *14*, 2000215.
- [24] J. Bonse, S. V. Kirner, J. Krüger, in *Handbook of Laser Micro- and Nano-Engineering* (Ed: K. Sugioka), Springer, Cham, **2021**, pp. 879–936, https://doi.org/10.1007/978-3-030-63647-0_17.
- [25] X. Tong, L. Zhu, K. Wang, Z. Shi, S. Huang, Y. Li, J. Ma, C. Wen, J. Lin, *Acta Biomater.* **2022**, *142*, 361.
- [26] V. Azar, B. Hashemi, M. Rezaee Yazdi, *Surf. Coat. Technol.* **2010**, *204*, 3546.
- [27] M. M. Lohrengel, *Mater. Sci. Eng.: R: Rep.* **1993**, *11*, 243.
- [28] C. E. Marino, E. M. Oliveira, R. C. Rocha-Filho, S. R. Biaggio, *Corros. Sci.* **2001**, *43*, 1465.
- [29] A. Karambakhsh, A. Afshar, P. Malekinejad, *J. Mater. Eng. Perform.* **2012**, *21*, 121.
- [30] Z. J. Liu, X. Zhong, J. Walton, G. E. Thompson, *J. Electrochem. Soc.* **2016**, *163*, E75.
- [31] D.-S. Kong, J.-X. Wu, *J. Electrochem. Soc.* **2008**, *155*, C32.
- [32] L. Moriau, M. Bele, Ž. Marinko, F. Ruiz-Zepeda, G. Koderman Podboršek, M. Šala, A. K. Šurca, J. Kovač, I. Arčon, P. Jovanovič, N. Hodnik, L. Suhadolnik, *ACS Catal.* **2021**, *11*, 670.
- [33] M. E. Orazem, B. Tribollet, *Electrochemical Impedance Spectroscopy*, Wiley, Hoboken, NJ **2008**.
- [34] K. H. Cheung, M. B. Pabbruwe, W.-F. Chen, P. Koshy, C. C. Sorrell, *Mater. Chem. Phys.* **2020**, *252*, 123224.
- [35] M. Metikos-Huković, A. Kwokal, J. Piljac, *Biomaterials* **2003**, *24*, 3765.
- [36] A.-M. Kietzig, S. G. Hatzikiriakos, P. Englezos, *Langmuir* **2009**, *25*, 4821.
- [37] C. Florian, R. Wonneberger, A. Undisz, S. V. Kirner, K. Wasmuth, D. Spaltmann, J. Krüger, J. Bonse, *Appl. Phys. A* **2020**, *126*, 266.